



HAL
open science

Three-dimensional skeletonization and symbolic description in vascular imaging: preliminary results.

Leslie Verscheure, Laurent Peyrodie, Anne-Sophie Dewalle, Nicolas Reyns, Nacim Betrouni, Serge R. Mordon, Maximilien Vermandel

► **To cite this version:**

Leslie Verscheure, Laurent Peyrodie, Anne-Sophie Dewalle, Nicolas Reyns, Nacim Betrouni, et al.. Three-dimensional skeletonization and symbolic description in vascular imaging: preliminary results.. International Journal of Computer Assisted Radiology and Surgery, 2013, pp.233-46. hal-01181350

HAL Id: hal-01181350

<https://hal.science/hal-01181350>

Submitted on 30 Jul 2015

HAL is a multi-disciplinary open access archive for the deposit and dissemination of scientific research documents, whether they are published or not. The documents may come from teaching and research institutions in France or abroad, or from public or private research centers.

L'archive ouverte pluridisciplinaire **HAL**, est destinée au dépôt et à la diffusion de documents scientifiques de niveau recherche, publiés ou non, émanant des établissements d'enseignement et de recherche français ou étrangers, des laboratoires publics ou privés.

Three dimensional skeletonization and symbolic description in vascular imaging: preliminary results.

Verscheure L.^{1,2,3}, Peyrodie L.^{2,3}, Dewalle A.S.^{1,2}, Reyns¹ N., Betrouni N.¹, Mordon S.^{1,2}, Vermandel M.^{1,2}

¹ Inserm U703, Université Lille 2, CHRU Lille, 59120 Loos, FRANCE

² PRES Université Lille Nord de France

³ LAGIS CNRS UMR 8146, Université Lille 1, 59655 Villeneuve d'Ascq, FRANCE

Abstract:

Objective

A general method was developed to analyse and describe tree-like structures needed for evaluation of complex morphology, such as the cerebral vascular tree. Clinical application of the method in neurosurgery includes planning of the surgeon's intraoperative gestures.

Method

We have developed a 3D skeletonization method adapted to tubular forms with symbolic description. This approach implements an iterative Dijkstra minimum cost spanning tree, allowing a branch-by-branch skeleton extraction. The proposed method was implemented using the laboratory software platform (ArtiMed). The 3D skeleton approach was tested on simulated data and preliminary trials on clinical datasets mainly based on magnetic resonance image acquisitions.

Results

A specific experimental evaluation plan was designed to test the skeletonization and symbolic description methods. Accuracy was tested by calculating the positioning error and robustness was verified by comparing the results on a series of 18 rotations of the initial volume. Accuracy evaluation showed a Hausdorff's distance always smaller than 17 voxels and Dice's similarity coefficient greater than 70%.

Conclusion

Our method of symbolic description enables the analysis and interpretation of a vascular network obtained from angiographic images. The method provides a simplified representation of the network in the form of a skeleton, as well as a description of the corresponding information in a tree-like view.

Key words: Medical imaging, vascular network, angiography, 3D skeletonization, symbolic description

1. Introduction

Symbolic description enables a summary to be made of an object observed via imaging, by describing its basic structures (e.g., connected components, branches of vascular trees, pixels, etc.) and the relations existing between its structures. In contrast to segmentation (which only allows a pixel to be classified as "in" or "out" of the object), symbolic description provides an environment in which the object is described according to a hierarchy enabling the exploration of its characteristics ($[[[\text{pixel} \in \text{branch}] \in \text{connected component}] \in \text{vascular network}] \in \dots$, etc.).

The human body contains a wide variety of elements which have a tree-like structure with a descending hierarchical organization (mother branches splitting to children branches). The

relevance of studying such structures using symbolic description approaches has already been shown for different areas.

In 1993, Gerig et al, [1] proposed an extraction method for 3D structures, in order to represent them using a symbolic approach, where the topological and geometrical information is represented in a tree-like form.

Later, in 2001, Bullit et al [2] highlighted the importance of knowing the relationships between the different branches of the cerebrovascular tree. Their study centered on the neurosurgical context of lower neck tumor resection, where the use of a clamp interrupted blood flow. It showed that understanding the relationships between the different vessels enabled cerebral perfusion to be anticipated and planned for during the operation.

More recently, Megalooikonomou et al [3] have presented a method for characterizing, classifying, and analyzing the similarities of tree-like structures in medical images. Using clinical data obtained from X-ray galactograms, they studied the branching of the lactiferous ducts, combining symbolic representation by graph with “text-mining” techniques. They suggest expanding the potential field of application to the study of links between the form of tree-like structure and the corresponding pathology.

In general, symbolic description has many applications. In the introduction to their article, Palagyi et al [4], highlight its use in, for example:

- virtual navigation (e.g., bronchoscopy or endovascular procedures), where a descriptive summary of the data allows the treatment linked to the simulation to be optimized
- exploration of complex structures (e.g., cerebral or hepatic vascular networks), which can be simplified as a result of navigation on a graph
- quantitative analysis of tubular forms (e.g., measurement of the vascular lumen or wall thickness)
- etc. (this list is not exhaustive)

The implementation of symbolic description usually follows an identical plan, in which the description is obtained after the extraction of data (binarization) and a skeletonization [4-7]. However, no matter the location nor the application, the root of the problem remains in the skeletonization. Much has been written about this subject, including reviews covering methodology [8-17], and its applications in medical imaging [18-26].

In this article, we concentrate especially on the whole cerebral vascular tree for which there is still very few references [1, 2, 27-29] despite the possible applications. Once the algorithm fully validated, it is expected to be applied in stereotactic neurosurgery. The main application is focused on finding the optimal and safest optical fibre path for brain interstitial photodynamic therapy [30].

For this location, we studied an iterative minimum cost spanning tree method based on Dijkstra’s algorithm [31]. This algorithm is especially interesting for our application as the search for the centerline uses the notion of the graph. Finally, the main novelty of our methodology is the application of Dijkstra’s algorithm to both skeletonize and describe the brain vascular tree.

The first part of this article describes the modalities of vascular imaging used in our application. We also describe how we implemented the skeletonization algorithm.

In the second part, we present a new evaluation plan for skeletonization, in which we introduce the use of digital phantoms, as well as tests on clinical data. Finally, we present and analyze the results.

2. Material and methods

As Palagyi et al [4] have noted, an overall solution for skeletonization adapted to all types of locations or forms does not seem to exist. By concentrating on their pulmonary airway tree application, these authors resolved certain difficulties [4], but problems remain for other applications. These problems are mainly linked to the properties defining the skeleton [32]:

- **Thickness:** the skeleton must have a unitary thickness (one voxel)
- **Position:** the skeleton is ideally positioned at the center of the forms
- **Homotopy:** the median axis has exactly the same number of connected components, and each component has the same number of holes as the initial form
- **Stability:** when the skeleton calculation is done by thinning, all or part of the skeleton should not be able to be eroded again once it has stabilized.

Two other properties can also be taken into consideration:

- **Invariance** by translation and rotation
- **Reversibility** of the skeleton: the form should be able to be reconstructed from the skeleton and the maximum ball rays.

For the vascular application that we are interested in here, we therefore chose to test a method that corresponds in part to the above properties (homotopy, position, thickness and reversibility). This method is mainly used for virtual colonoscopy, as it is particularly well adapted to tubular forms [31]. It is based on the construction of the Dijkstra's minimum cost spanning tree.

Our implementation followed the plan generally accepted in the literature for skeletonization and tree extraction, represented Figure 1.

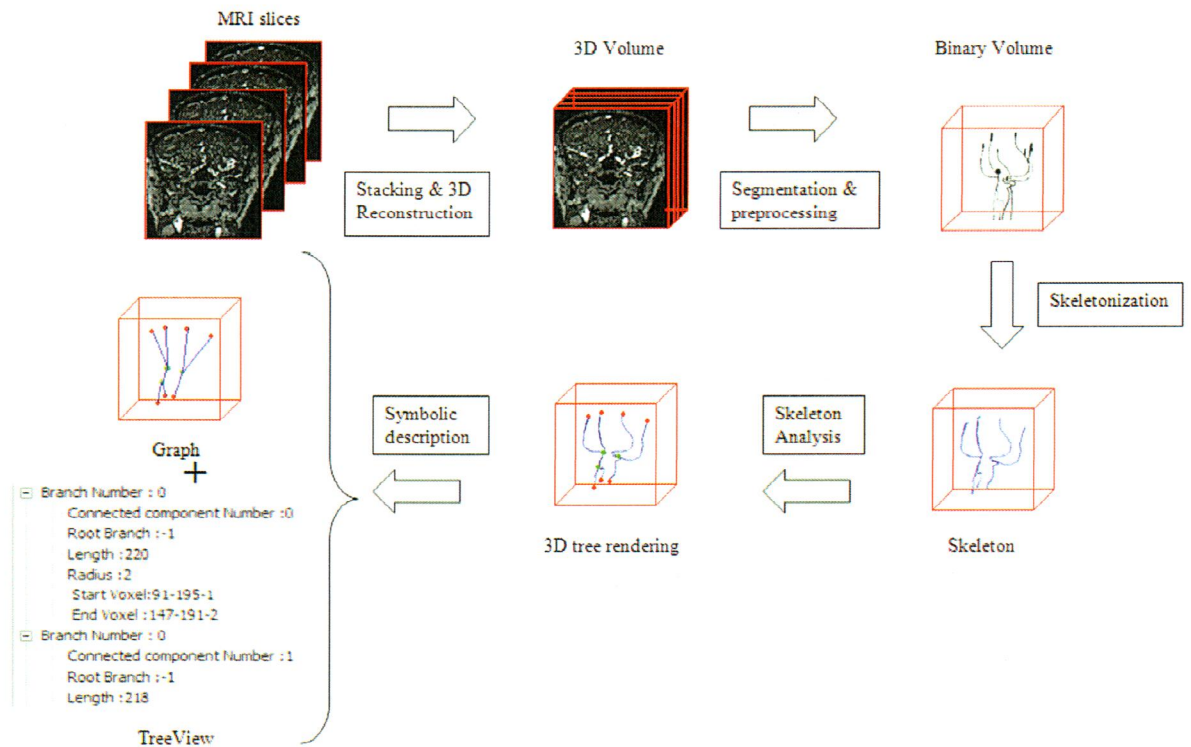


Figure 1: Summary of the different stages of symbolic description.

The main topic of this paper being skeletonization and symbolic description, for our purpose the correct segmentation is considered to be given independently on method use. Therefore, any segmentation techniques could be used in this symbolic description method. In this study we have used a specific segmentation approach, which relies on the Maximum of Intensity Projection [33]. The efficiency of this approach was previously evaluated for different modalities [34, 35] and especially for different MR angiography sequences[36, 37].

2.1. Skeletonization using Dijkstra's tree

Skeletonization is the standard method used to determine a form's centerlines. In continuous or discrete fields, the choice of methods is fairly varied. However, one of the problems that is frequently encountered is the presence of surfaces or small barbules (especially of clusters of voxels at the level of junctions) in a skeleton that we would prefer to be thin [38]. Using iterative Dijkstra's minimum cost spanning tree to extract the thin branches can solve this constraint.

This solution for skeletonization, introduced by Wan et al [31] for application in virtual colonoscopy, has also been used by Hassan et al in the setting of vascular analysis of aneurysms [27, 39]. However, in these articles, the authors used this skeletonization stage with the aim of extracting only one part of the tree: the central colonic axis in [31] or the branches affected by an aneurysm with the intent of carrying out "Computed Fluid Dynamic simulations" [27, 39].

In the first case, the technique used only allowed the extraction of the principal centerline. In order to extract the first generation branches, the authors therefore proposed an extension to the algorithm from this centerline [31].

In our context, this extension proved to be inadequate, and we therefore propose a new extension in order to skeletonize the tree down to the most distant vessels. In this generalization, it is advisable to reiterate the process for each first generation branch associated with the centerline.

Our method aims to extract the skeleton in a recursive manner from an iterative Dijkstra minimum cost-spanning tree. From the longest branch of the vascular structure the main centerline was first extracted. Then, from the main centerline, the child centerlines being directly connected were identified. Finally, the process was reiterated for each newly detected child centerline.

2.1.1. Construction of the iterative minimum cost spanning tree

In graph theory, Dijkstra's algorithm [40] is used to resolve the shortest path problem. It applies to a related graph in which the weight linked to the edge is nonnegative

Firstly, the volume had to be converted into a weighted 3D graph. The centre of each voxel therefore represented a vertex in the graph and the relations of 26-neighborhood between the voxels are symbolised by the edges of the graph.

In our case, the weight attributed to each vertex depends on the distance with respect to the boundary (Distance from Boundary [DFB]). The further the voxel under consideration is from the boundary, the higher the probability is that it will be on the centerline. To calculate the DFB, we calculated the smallest Euclidean distance between each voxel and the boundary points (boundary points refer to voxels with at least one neighbour belonging to the background).

To describe the algorithm, we define the following variables:

- vertex S: source vertex
- vertex C: node being processed at a given iteration
- N/N_i represents a neighbor of vertex C
- EndPointList/JunctionList: lists storing the endpoints and the junctions of the detected centerlines, respectively.

In our implementation Source vertex definition is automatic. Indeed, the root is obviously at one end of the tree structure. Thus from an arbitrary voxel (centered on the volume) and from which the distance to all the form's voxels is calculated, the point furthest away refers as the source vertex

Each vertex has several properties:

- pathlink: indicates the link with the neighbor
- Distance from source (DFS): is the distance from the vertex to the source vertex weighted according to the DFB
- the state of the vertex indicates if it has already been processed during an iteration (Mark (C) = *true* if processed, otherwise *false*).

From these definitions and using a heap to process the vertices, the algorithm is described Figure 2:

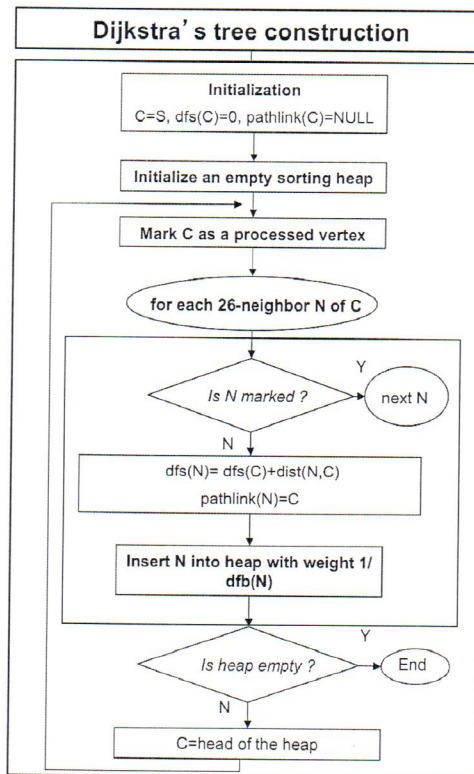


Figure 2: Algorithm for the calculation of Dijkstra's tree, where $dist(N,C)$ is the Euclidean distance from N to C

2.1.2. Main vessel centerline and its child centerlines extraction using Dijkstra's tree

Let us define a centerline be a set of vertices from the Dijkstra's tree. Thus, the centerline extraction algorithm was based on the movement through the tree from the vertex at maximum DFS up to the Source point. By using each vertex's pathlink property and considering the tree as an oriented graph (in which reversing is impossible), the main centerline was defined as the longest branch. The identification of the vertex of the maximum DFS is enough to enable a gradual retracing up to the Source vertex (chosen in section 2.2), via the pathlinks.

The extraction of first generation child centerline was based on the following stages:

- sweeping through the main centerline by retracing from E to S (see Figure 3) along the pathlinks
- for each vertex C of the main centerline, looking at its neighbors (apart from those belonging to the main centerline) and finding the N_i 's which have their pathlink at C (e.g., $pathlink(N_i)=C$)
- for every N_i , searching for all its linked vertices V (either directly $pathlink(V)=N_i$ or indirectly $pathlink(pathlink(...pathlink(V)))=N_i$).
- finding the vertex T_i which had the largest DFS of all the vertices V
- storing T_i as the tip of a child centerline (i.e., $T_i \in EndPointList$) if $DFS(T_i)$ was above a fixed threshold L (L is a threshold used to prevent from noise to be detected as a centerline).
- storing C as being a junction (i.e., $C \in JunctionList$)

Figure 3 shows an example of searching for a branch, in 2D. Figure 4 summarizes the method.

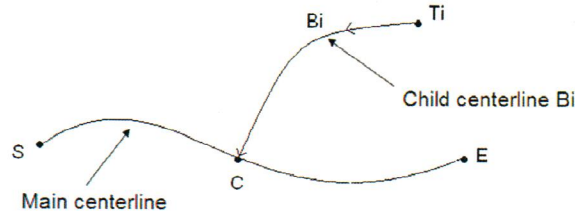


Figure 3: Extraction of the main centerline and its child centerlines. S and E are the source voxel and the end voxel, respectively; C is the current voxel, and Ti is the end voxel of a secondary branch Bi.

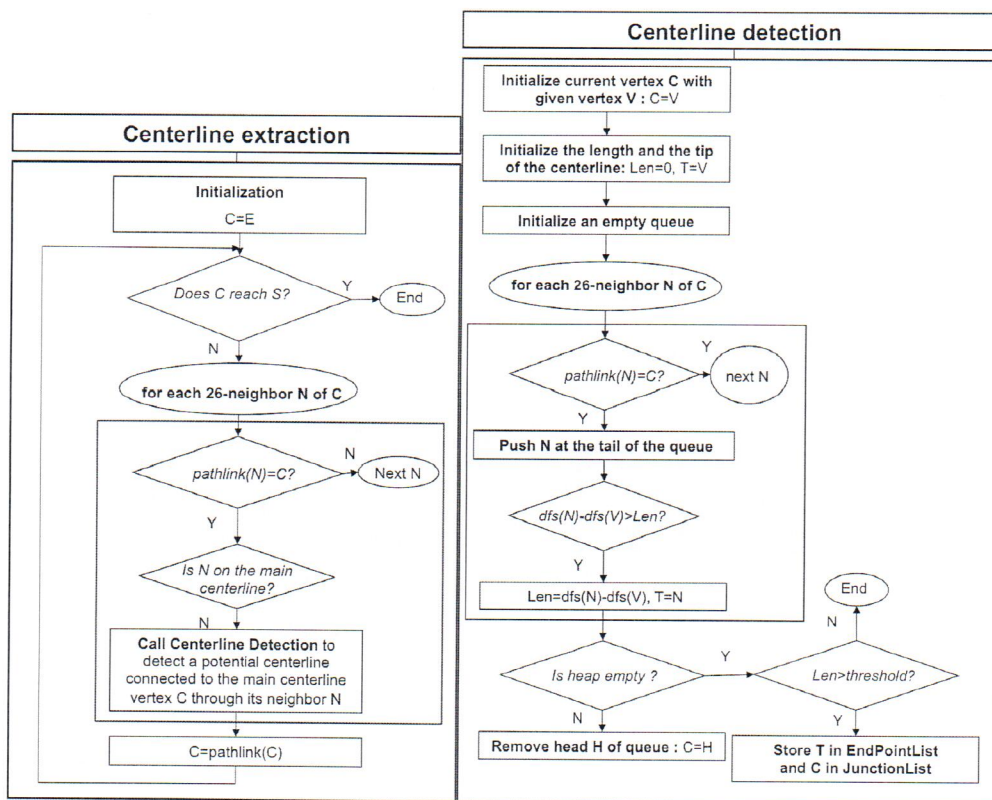


Figure 4: Extraction of centerlines using Dijkstra's tree. Centerline extraction makes use of centerline detection to detect the centerline indirectly connected to the current vertex.

A unique characteristic of our algorithm is the storing of the tips of the centerlines, as appropriate, in the EndPointList or JunctionList. This enables the simultaneous interpretation of the information gathered, both for the preliminary stages of symbolic description and for skeletonization.

After this stage, we extracted the first generation child centerlines, i.e., the child centerlines directly linked to the main centerline. For the extraction of more distal branches centerlines, we chose to implement the algorithm in a recursive manner; this enabled the detection of 2nd, 3rd, and later generations, for every extracted centerline. The implementation of this new overall method is illustrated in Figure 5.

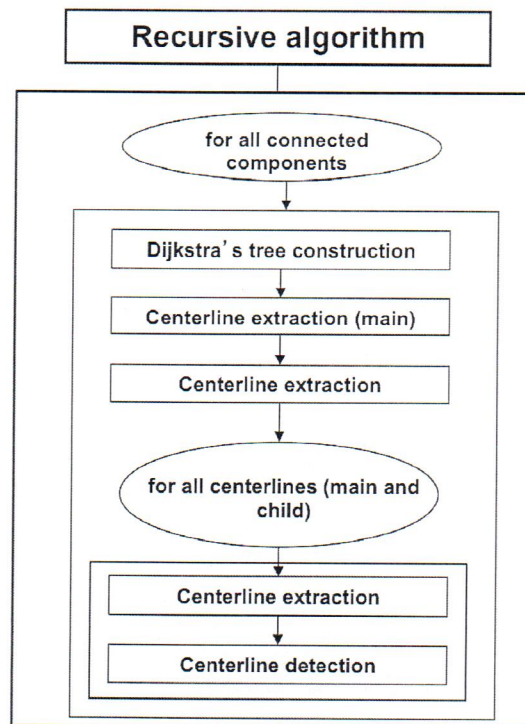


Figure 5: Recursive skeletonization

The extraction of the 2nd generation branches centerline and onwards was based on the same principle as for the 1st generation. The minor modifications required in the algorithm were:

- sweeping the child centerline from T_i to C while retracing from E towards S along the pathlinks
- storing T_i as the centerline tip (i.e. $T_i \in \text{EndPointList}$) if $\text{DFS}(T_i)$ was above a fixed threshold L (the length of the centerline was its number of vertices).

2.2 Identification of particular points

At this stage, the skeleton was defined from the vertices and centerline previously obtained.

On a skeleton, we can identify three types of points: the endpoints (which have only one 26-neighbor), the junctions (which have more than two 26-neighbors) and the skeleton points (which have exactly two 26-neighbors) Thus from this specific points, the different vascular segments or branches can be easily identified.

There are 3 cases if we consider the skeleton to be oriented:

- a branch beginning with an endpoint and ending with a junction: mother branch E-J
- a branch beginning with a junction and ending with a junction: intermediate child branch J-J
- a branch beginning with a junction and ending with an endpoint: end child branch J-E.

Usually, the symbolic description is made from the analysis of the skeleton. In our case, we already had the skeleton's characteristic voxels in the EndPointList and the JunctionList from the analysis of Dijkstra's tree as described above. Indeed, endpoints and junction analysis is

performed simultaneously with the extraction through the application of Dijkstra's algorithm. This specificity of the algorithm could result in an appreciable reduction in the manipulation of the voxel matrix, and thus reduces calculation time.

As our algorithm is recursive, we extract only the E-J centerline. Each centerline then has to be divided into mother, intermediate centerline or end centerline, according to the cases described above.

2.3 Partitioning of the vascular tree and associated measures

From the skeleton and the centerlines previously extracted, we wanted to link every voxel to a centreline from the skeleton. The method took the segmented volume and the data gathered from the skeletonization (i.e., the skeleton and particular points) as input. As output, the result was a volume for which every voxel was labelled, depending on the branch it belonged to.

Partitioning was carried out automatically by calculating the distances between every voxel in the volume extracted by segmentation and the voxels in the skeleton. For a given voxel, we searched for the nearest skeletal voxel (which had already been labelled during the skeletonization). The unlabelled voxel was attributed the same label as the skeletal voxel.

Figure 6 shows the result obtained on an artificial volume and a vascular network:

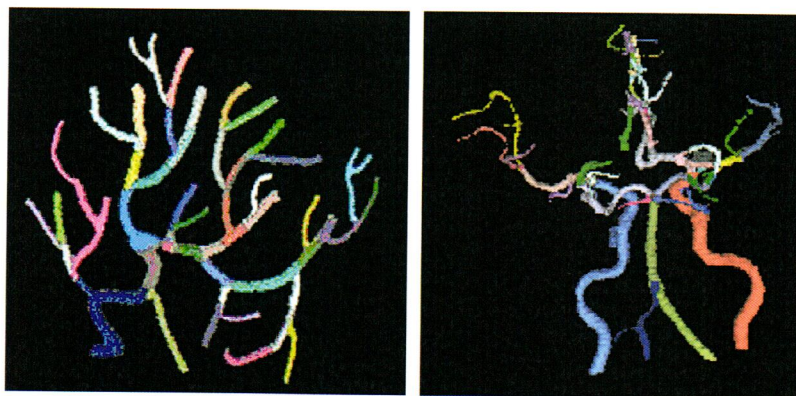


Figure 6: Partitioning of an artificial volume and a vascular network taken from clinical data

Using the formula for the volume of a cylinder as an approximation, this stage also allowed us to calculate the theoretical radius of each branch. Once the voxels were labelled, we knew the list of those belonging to each branch. Assuming that the vessels could be modelled as cylinders, all that was needed was to calculate the volume corresponding to the group of these voxels and the number of voxels in that branch of the skeleton. These values correspond to the volume (number of voxels \times size of voxel) and the length (number of voxels in the branch) respectively of the theoretical cylinder representing the vessel. Obviously, this radius calculation is only a rough approximation since it has been demonstrated that the venous network does not fit a cylinder or tubular model [41] and the different arteries cannot be considered as tube with constant diameter [42]. The constant radius model is used here as illustration and a more suitable approach could be further investigated specially when dealing with vessels with radius smaller than the voxel size [43].

2.4 Image datasets

The approach described in this paper was evaluated on two different datasets including digital phantom and clinical images. Indeed, in the absence of ground truth concerning clinical data,

we tested the accuracy of our method on simulated data, using a digital phantom constructed using Matlab© (The MathWorks™, <http://www.mathworks.fr>).

a) Simulated data

We created an interface using Matlab (Figure 7 (a)) which allowed us to generate digital models from a reference skeleton (a spline). Secondary branches were connected to a principal branch, forming the skeleton of a tree-like structure. A volume was then constructed from the skeleton and the given branch diameters.

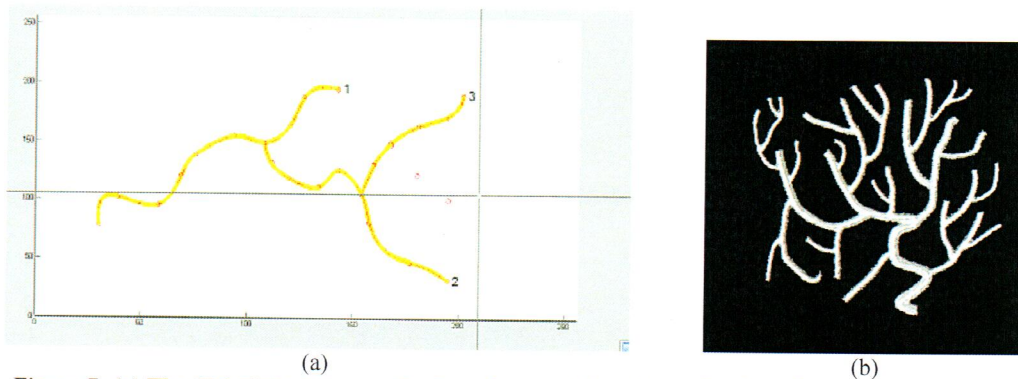


Figure 7: (a) The digital model's creation interface enabling the evaluation of the skeletonization algorithm and the symbolic description (b) Resulting digital model

The digital model built up in this way, Figure 7 (b), allowed us to precisely define the characteristics of the skeleton under research: the point coordinates, the radii, the length of branches, relationships, etc..

b) Clinical data

The clinical datasets were images taken from different MRA and 3DRA sequences. The sizes were 345x259x142 (MRI, Time Of Flight, voxel size 0.47x0.47x0.72), 272x188x270 (MRI, Gadolinium Contrast Enhancement 0.48x0.48x0.65 mm³), 256x256x150 (MRI, 3D Phase Contrast, voxel size 0.5x0.5x1mm³) and 256x256x256 (3D X ray Rotational Angiography, voxel size 0.29x0.29.0.29 mm³)

	Initial volume	Skeleton	Reconstructed volume
(a)			
(b)			




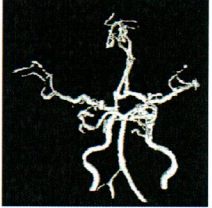

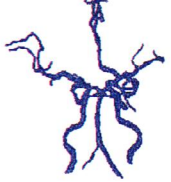
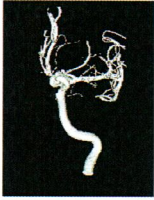


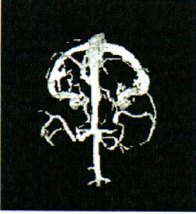


(c) (TOF MRA)			
(d) (MRA Gd)			
(e) (3DRA)			
(f) (PC MRI)			

Figure 8: Qualitative results (a-b) Digital phantoms, (c) to (f) Clinical cases

Figure 8 shows the results on digital phantoms (a-b) and on four clinical cases (c – TOF MRA, d - MRA Gd enhanced, e – 3D Rotational Angiography and f – Phase Contrast MRI). The initial volume is shown, along with the skeleton extracted using our method, and the volume reconstructed from the skeleton.

The skeletonization approach copes with both arteries and veins, thus the clinical data proposed includes arterial system imaging (c, d and e on Figure 8) and venous system (f on Figure 8). Nevertheless, we can observe that the oriented graph approach with the Dijkstra's algorithm may lead to limitations since some parts of the circle of Willis are missing (c and d on figure 8).

3 Experimental methods

Few methods exist for the evaluation of skeletonization algorithms. However, Palagyi et al [4] have proposed an interesting plan for the quantitative evaluation of skeletonization. Using a physical phantom, a digital phantom, and in-vivo acquisition, their experimental plan enables the number of branches detected, the positioning error, and the diameters, lengths, and volumes of the detected branches to be verified. We adopted approximately the same evaluation strategy in our study.

3.1. Validation criteria

3.1.1. Accuracy

To verify the accuracy of our solution for skeletonization, we compared the skeleton endowed with the characteristics extracted using our method with a theoretical skeleton. This involved examining the skeleton's positioning error and the precision of the symbolic description information.

3.1.2. Robustness

The second evaluation criterion was the robustness of the symbolic description, i.e., the extent to which the results remain stable after any disruption. The conditions under which images are acquired cannot be exactly the same (especially concerning the orientation of the patient's head). However, in images from the same patient, the symbolic description should give the same result. We therefore decided to observe how the method dealt with a series of rotations.

3.2. Experimental plan

3.2.1. Accuracy

The use of digital model allowed us to have the geometric information concerning the branches, and as a result, we had the ground truth associated with the volume created (the spline used to build the volume and related information). We then estimated the positioning error, calculated by a hyperbolic Hausdorff distance [44] between the reference skeleton and the obtained skeleton.

To this evaluation, we added the calculation of the Dice Similarity Coefficient (DSC) between the original volume and the reconstructed volume, which allowed us to assess the skeleton's reversibility properties.

The reconstructed volume resulted from information from the skeleton and the symbolic description. For each point in the skeleton, we thus formed a ball of radius which corresponded to the Euclidean distance between this point and the edge of the nearest volume (DFB).

3.2.2. Robustness

Following Palagyi et al's approach [4], we rotated each volume studied by 5° from -15° to 15° . This enabled us to study the following characteristics of the branches by opposing the values obtained with or without rotation:

- length
- volume
- surface
- radius

For the statistical analysis, we used the Bland-Altman approach [45, 46] for evaluating the agreement between two methods. This method is used to compare two methods in the absence of a gold standard. The aim is to characterize the coherence of the results obtained by the new method compared with those using the other method. We evaluated the reproducibility by comparing the results obtained from the original volume with those of the 18 rotations.

4 Results

The algorithms were implemented using a software platform owned by ArtiMed laboratory, and developed in Borland C++. The manipulations were carried out on a personal computer (processor: AMD 2.4 GHz- RAM: 2Gb). The computation time was less than 30 seconds for a matrix of 256x256x256 voxels with 140,000 voxels belonging to the vascular tree.

4.1. Accuracy

As previously mentioned, we indicated the hyperbolic Hausdorff distance between the skeleton obtained using our approach and the native skeleton of the digital phantom. In addition, for the 18 rotations of the Matlab volume, we determined the mean DSC between the reconstructed volume and the original volume.

Figure 9 shows the visual and quantitative results obtained on two digital phantoms using our algorithm for model generation. The images represent the superimposition of the initial skeleton on the calculated skeleton, and the initial volume superimposed on the volume obtained after post-skeletonization reconstruction. The numbers given are the mean values of the hyperbolic Hausdorff distance and the DSC from the 19 volumes.

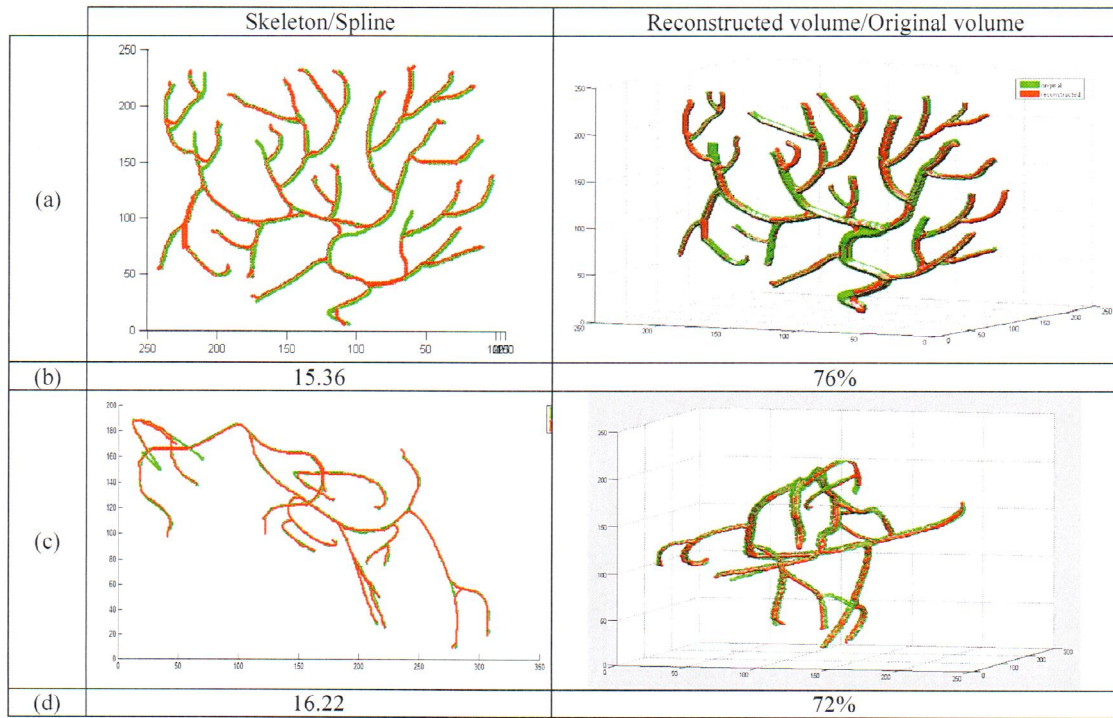


Figure 9: Results on digital phantoms (a-c) Superimposition (reference in green, results in red)
(b-d) Numerical results: hyperbolic Hausdorff distance and Dice Similarity Coefficient

4.2. Robustness

For each branch extracted by symbolic description, we compared a given characteristic of the initial volume (length, radius or number of voxels in the branch) with the same characteristic in the reconstructed volume after rotation and extraction. For each rotation and each branch, we therefore obtained the percentage error of the characteristic studied, denoted by $err_{val_{i,j}}$, in the following way:

For $i=1, \dots$, number of branches
 For $j=1, \dots$, number of rotations

$$err_val_{i,j} = \frac{|val_{init} - val_{rot_j}|}{val_{init}} * 100 \quad \text{Eq. 1}$$

end
 end

For each characteristic, we then calculated the mean error on all rotations on each branch, using:

For $i=1, \dots$, number of branches

$$my_err_val_i = \underset{j=1, \dots, \text{number of rotations}}{\text{mean}} (err_val_{i,j}) \quad \text{Eq. 2}$$

end

Finally, the mean percentage error for each characteristic was described by:

$$\begin{aligned} mean_ \%_error &= \underset{i}{\text{mean}} (m_err_val_i) \\ sd_error &= \underset{i}{\sigma} (m_err_val_i) \end{aligned} \quad \text{Eq. 3}$$

Table 1 shows the mean percentage errors \pm SD for the reproducibility of the characteristics studied between the original volume and the 18 volumes obtained by rotation.

% error	Simulated volume (a)	Simulated volume (b)	Clinical case (c)	Clinical case (d)
number of voxels	8.7 \pm 4.07	8.9 \pm 4.6	9.4 \pm 4.4	14.9 \pm 10.7
length	3.8 \pm 3	7.2 \pm 3.4	5.4 \pm 2.2	12.5 \pm 7.6
radius	13 \pm 8	4.9 \pm 2.3	11.1 \pm 10.7	12.9 \pm 8

Table 1 : Reproducibility of results: quantitative data

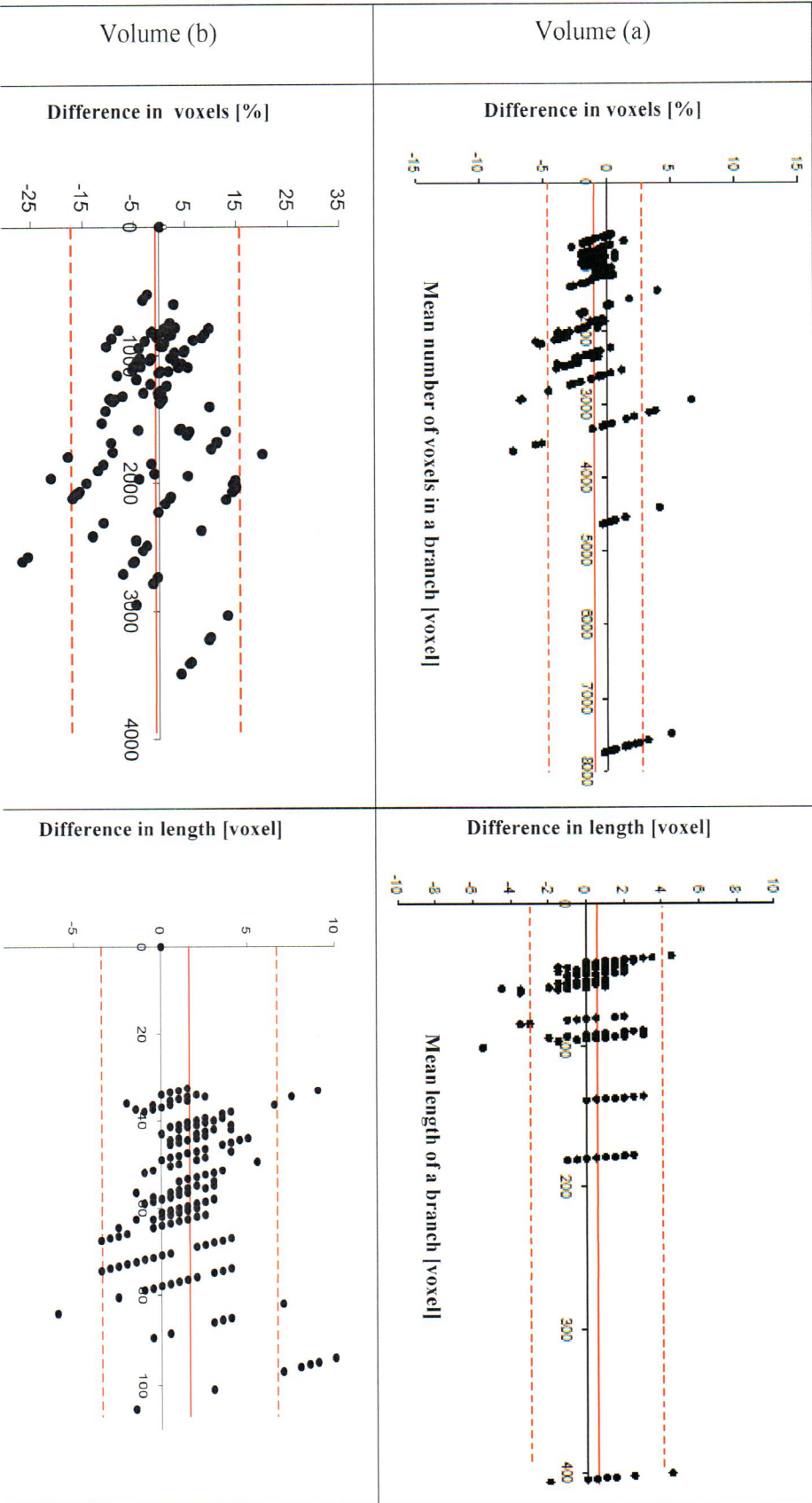
The reproducibility indices for the radius and the number of voxels on the simulated data are shown in Figure 10; the corresponding indices for two clinical cases are shown in Figure 11. The Bland-Altman plots indicate the 95% Confidence Intervals.

For each case, the mean difference between the estimates obtained from the 2 methods is represented, according to the mean of the two estimates, m_1 and m_2 . When there is no additional information, this mean represents the best estimate of the true value of the parameter. In our case, the m_1 estimate was replaced by the values obtained for the initial volume, and the m_2 estimate took the values resulting from each rotation alternately.

On this type of plot, the mean of the differences corresponds to the mean bias between the two methods. If one hypothesizes that the differences follow a normal distribution, 95% of the measures will be between the mean value $\pm 1.96 \times$ SD of the differences. According to this interval's range, one can determine if the two methods are interchangeable. For example, a maximum tolerable value of difference can be fixed, so that the methods can be used to replace one another.

We then studied the reproducibility of the characteristics (branch length, number of voxels per branch and the radius of branches for the 19 volumes [initial volume + 18 rotations]) according to the rotations.

Finally, on figures 10 and 11, we can observe that 95% of the points are within the confidence interval demonstrating a good robustness with regard to the volume orientation before skeletonization and symbolic description.



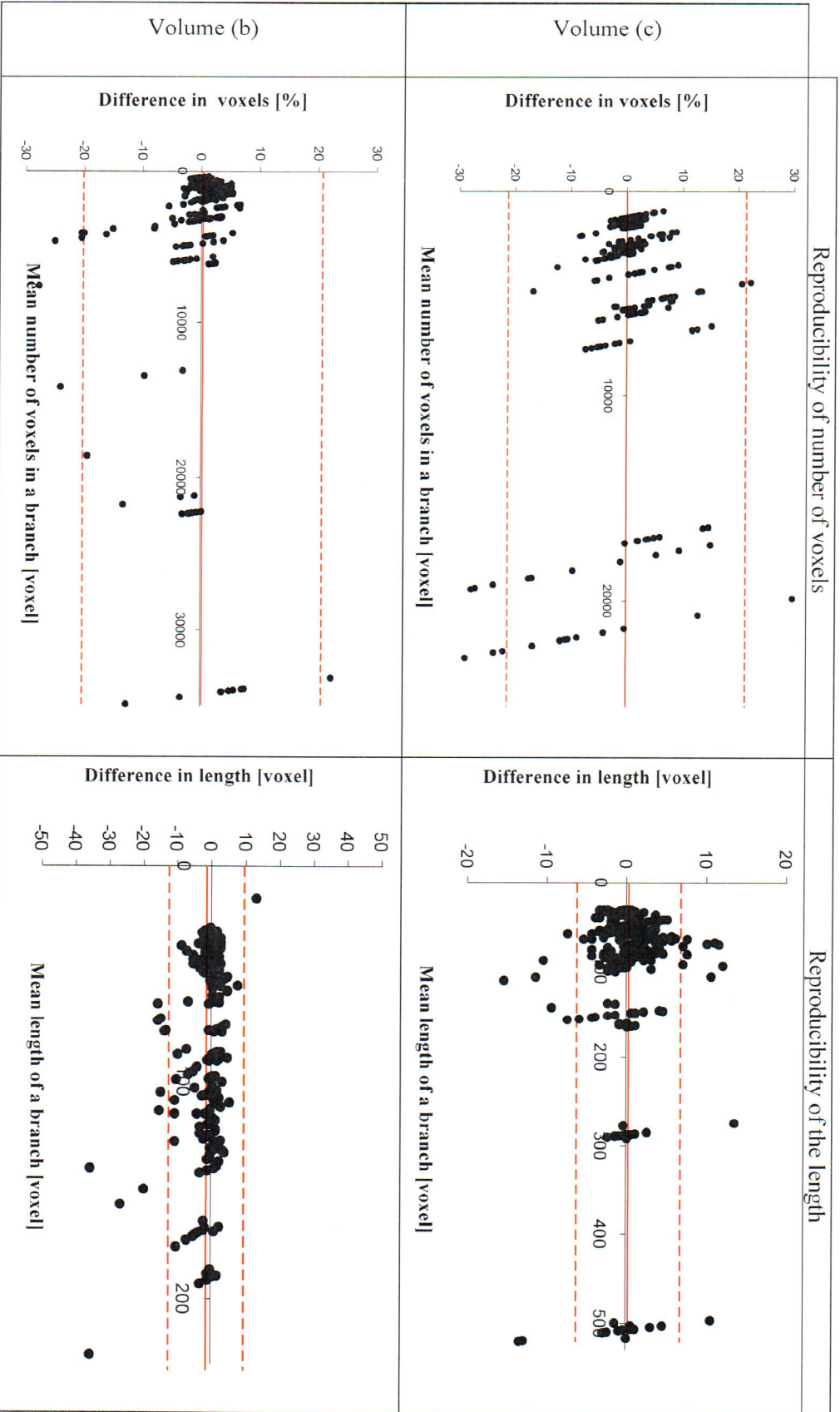


Figure 11: Reproducibility of results for clinical data: Bland-Altman plot

5. Discussion

The investigations on symbolic description presented in this paper are within the context of neurosurgery. According to recent advances in brain photodynamic therapies (PDT) [30, 47], the development of a planning system to deliver optimal dose with optical fibers in stereotactic conditions becomes crucial to include PDT in the management of high-grade glioma. The symbolic description aims to answer the problem of fibers positioning. The problem is strictly the same as in the Stereo-Electro-Encephalogram procedure (SEEG) [48, 49] in the presurgical evaluation of focal epilepsy. During SEEG procedure, the risk of collision of an electrode and vessels is extremely high. A strategy based on symbolic description is expected to minimize the risk by computing a risk of collision map according to the path of the optical fibers and the description of the brain vascular network.

The symbolic description we describe is based on the construction of the Dijkstra's tree. The 3D segmentation approach used in the methodology has already been described [50, 51]. Nevertheless, our approach enables the use of any segmentation technics to be further explored. For example, recent advances in hepatic vessel segmentation [52] could also be investigated and transferred to our symbolic description approach as these hepatic and brain localizations are both dealing with the same level of complex vascular structure.

The method that we have proposed for the extraction of centerlines and the descriptive analysis of tubular objects has several interesting properties. Firstly, the basic tool for the calculation of the skeleton is the construction of Dijkstra's tree. This enables a thin result to be obtained (1 voxel thick) without the need of a pruning stage, as a length limit is applied during the branch detection phase. Secondly, the use of this approach to skeletonization allows a preliminary description to be carried out "during the extraction". The iterative detection of the skeletal branches enables a first analysis of the tree structure.

The accuracy of our method was evaluated only on simulated data, for which we knew the ground truth of the construction. We could see the good superimposition obtained between the skeleton and the construction spline, with a hyperbolic Hausdorff distance of 15 voxels. We can conclude that, on the simulated data, the method is satisfactory, as the value of 15 (which notably reveals non-detection of the smallest branches) is highly acceptable, given the severe criteria chosen.

In the same way, we evaluated the accuracy using the skeleton's reversibility criteria, by superimposing the original volume on the reconstructed volume. The DSC was chosen to quantify the superimposition, and the mean value obtained was 76%. Taking into account our spherical reconstruction model, and the use of the mean radial value of each branch, we conclude that the index of 76% indicates good reversibility. In fact, the theoretical index calculated for the reconstruction method used after symbolic description versus the volume obtained by the model generator gives a maximum value of 90.7%. This value highlights the shortcomings in our reconstruction model, but enables the value obtained during the experiments to be more clearly analyzed and understood.

Turning to the robustness, we first presented the means and SDs of the percentage errors for each characteristic (length, volume and radius of the branches). Apart from that of the radius, the error SDs obtained were small and therefore highly satisfactory. Taking into account the characteristics extracted by symbolic description, the error obtained for the radius was not satisfactory; this error concerned the mean radius of a branch and did not take into account the variability which exists along the branches. However, no matter which characteristic was studied, the use of the Bland-Altman plots (figure 10 and figure 11) enabled us to observe that 95% of the points were within the

confidence interval, thus implying that the method was robust with regard to the volume orientation before skeletonization and symbolic description.

Obviously, we are aware of the small clinical database used here for the evaluation. However, as a preliminary study we focused our experiments on simulated data. The clinical data is mainly used to evaluate the portability of the approach in a multimodality context. A larger clinical images dataset and more realistic simulations should help to fix issues concerning the circle of Willis as illustrated on figure 8c and 8d. In [52], the authors proposed an interesting evaluation framework using a stereo lithography phantom designed from actual patient images. A similar evaluation framework will be assessed for our approach. Using MRI simulation from actual patient images will give access to a known ground truth with evaluation material closer to the clinical context.

6. Conclusion and future prospects

We have proposed a new approach to the extraction of the cerebral vascular tree based on the iterative calculation and analysis of the Dijkstra's minimum cost spanning tree. Furthermore, we have proposed a new evaluation framework adapted from [4]. This complete framework is adapted to all types of tubular forms (blood vessels, lactiferous ducts, the pulmonary network, etc.).

A DSC above 70% proves that the skeleton is reversible. In addition, the weak positioning error between the reference and the calculated skeleton indicates that the algorithm is robust. This leads us to conclude that the method is relevant for tree-like objects, and, in particular, satisfies the fundamental requirements needed for future clinical application. However, our approach has to be evaluated on a larger clinical database especially with images of the circle of Willis for which the oriented graph strategy could lead to limitations.

Our method of symbolic description enables the analysis and interpretation of a vascular network obtained from angiographic images. It provides a simplified representation of the network in the form of a skeleton, as well as a description of the corresponding information in the form of a tree-like view. It therefore creates an interaction between visual and descriptive information by linking these two representations of the network. This type of vessel representation may be of use in the development of new applications (e.g., in new Computational Fluid Dynamics models, the association of a subject's data with a vascular atlas, simulation of the vascular tree / neurosurgeon tools interactions...).

References:

- [1] G.Gerig, T.Kollera, G.Szekely, C.Brechbuhler, and O.Kubler, "Symbolic description of 3-D structures applied to cerebral vessel tree obtained from MR angiography volume data," *Proceedings of 13th International Conference on Information Processing in Medical Imaging, IPMI'93, ser.Lecture Notes in Computer Science*, vol. 687, pp. 94-111, 1993.
- [2] E.Bullit, S.Aylward, K.Smith, S.Mukherji, M.Jiroutek, and K.Muller, "Symbolic description of intracerebral vessels segmented from Magnetic Resonance Angiograms and evaluation by comparison with X-Ray Angiograms," *Medical Image Analysis*, vol. 5, pp. 157-169, 2001.
- [3] V.Megalooikonomou, M.Barnathan, D.Kontos, P.R.Bakic, and A.D.A.Maidment, "A representation and classification scheme for tree-like structures in medical images : analyzing the branching pattern of ductal trees in X-ray galactograms," *IEEE Transactions on medical imaging*, vol. 28, no. 4, pp. 487-793, 2009.
- [4] K.Palagyi, J. T. E.A.Hoffman, and M.Sonka, "Quantitative analysis of pulmonary airway tree structures," *Computers in Biology and Medicine*, vol. 36, no. 9, pp. 974-996, 2006.
- [5] Z.Chen, and S.Molloi, "Automatic 3D Vascular Tree Construction in CT angiography," *Computerized Medical Imaging and Graphics*, vol. 27, pp. 469-479, 2003.
- [6] V. Mohan, G. Sundaramoorthi, A. Stillman, and A. Tannenbaum, "Vessel segmentation with automatic centerline extraction using tubular tree segmentation," 2009.
- [7] Y. WANG, J. LI, and S. CHEN, "A Novel Method of Extracting 3D Blood Vessel Images Axis Based on Energy Constraint Equation," *Journal of Computational Information Systems*, vol. 7, no. 4, pp. 1319-1327, 2011.
- [8] C.Kirbas, and F.Quek, "A review of vessel extraction techniques and algorithms," *ACM Computing Surveys*, vol. 36, no. 2, pp. 81-121, 2004.
- [9] K.Krissian, G.Malandain, N.Ayache, R.Vaillant, and Y.Trousset, "Model based detection of tubular structures in 3D images," *COMPUTER VISION AND IMAGE UNDERSTANDING*, vol. 80, pp. 130-171, 2000.
- [10] K.Palagyi, and A.Kuba, "A 3D 6-subiteration thinning algorithm for extracting medial lines," *Pattern Recognition Letters*, vol. 19, no. 6, pp. 627, 1998.
- [11] L.Lam, S.W.Lee, and C.Y.Suen, "Thinning Methodologies -- A Comprehensive Survey," *IEEE Transaction on Pattern Analysis and Machine Intelligence*, vol. 14, pp. 869-885, 1992.
- [12] M.Maddah, A. A. Kusha, and H. S. Zadeh, "Efficient center-line extraction for quantification of vessels in confocal microscopy images," *Med.Phys.*, vol. 30, pp. 204-211, 2003.
- [13] P.Saha, B.Chaudhury, and D.Majumder, "A new shape-preserving parallel thinning algorithm for 3D digital images," *Pattern Recognition*, vol. 30, pp. 1939-1955, 1997.
- [14] S.Aylward, and E.Bullit, "Initialization, noise, singularities, and scale in height ridge traversal for tubular object centerline extraction," *IEEE Transactions on medical imaging*, vol. 21, pp. 61-75, 2002.
- [15] S.Bouix, K.Siddiqi, and A.Tannenbaum, "Flux driven fly throughs," International Conference on Computer Vision and Pattern Recognition, Madison, WI, 2003, pp. 449-454.
- [16] T. Saito, and J. Toriwaki, "A sequential thinning algorithm for three dimensional digital pictures using the Euclidean distance transformation," Proceedings, 9th Scandinavian Conference on Image Analysis (SCIA/95), Uppsala, Sweden, 1995, pp. 507-516.
- [17] D. Lesage, E. D. Angelini, I. Bloch, and G. Funka-Lea, "A review of 3D vessel lumen segmentation techniques: models, features and extraction schemes," *Med Image Anal*, vol. 13, no. 6, pp. 819-45, Dec, 2009.

- [18] I.Nystroem, "Skeletonization applied to magnetic resonance angiography images," *Proceeding of Medical Imaging*, vol. 3338, pp. 693-701, 2003.
- [19] J.Toriwaki, and K.Mori, "Distance transformation and skeletonization of 3D pictures and their applications to medical images," *Digital and Image Geometry, ser.Lecture Notes in Computer Science 2243*, pp. 412-429, 2001.
- [20] K. Mori, J. Hasegawa, J. Toriwaki, H. Anno, and K. Katada, "A fast rendering method using the tree structure of objects in virtualized bronchus endoscope system," *Lecture Notes in Computer Science*, vol. 1131, pp. 33-42, 1996, 1996.
- [21] K. Mori, J. Hasegawa, and Y. Suenaga, "Automated labeling of bronchial branches in virtual bronchoscopy system," *MICCAI'98*, 1998, pp. 870-878.
- [22] L.Antiga, B. E. Iordache, and A.Remuzzi, "Computational geometry for patient-specific reconstruction and meshing of blood vessels from angiography," *IEEE Transactions on medical imaging*, vol. 22, pp. 674-684, 2003.
- [23] S.Wan, A.Kiraly, E.Ritman, and W.Higgins, "Extraction of the hepatic vasculature in rats using 3-D micro-CT images," *IEEE Transactions on medical imaging*, vol. 19, pp. 964-971, 2000.
- [24] S.Wan, E.Ritman, and W.Higgins, "Multi-generational analysis and visualization of the vascular tree in 3D micro-CT images," *Computers in Biology and Medicine*, vol. 32, pp. 55-71, 2002.
- [25] S.Wood, A.Zerhouni, J.Hoford, E.A.Hoffman, and W.Mitzner, "Measurement of three-dimensionnal lung tree structures using computed tomography," *Application Physiology*, vol. 79, pp. 1687-1697, 1995.
- [26] T.Deschamps, and L.D.Cohen, "Fast extraction of minimal path in 3D images and applications to virtual endoscopy," *Medical Image Analysis*, vol. 5, pp. 281-299, 2001.
- [27] T.Hassan, Ev.Timofeev, T.Saito, H.Shimizu, M.Ezura, Y.Matsumoto, K.Takayama, T.Tominaga, and A.Takahashi, "A proposed parent vessel geometry-based categorization of saccular intracranial aneurysms: computational flow dynamics analysis of the risk factors for lesion rupture," *American Journal of Neuroradiology*, vol. 103, no. 4, pp. 662-680. Erratum in: *J Neurosurg*. 2005 Dec;103(6):1110., 2005.
- [28] A. Qi, and J. Xu, "Skeleton extraction of cerebral vascular image based on topology node," *3rd International Conference on Biomedical Engineering and Informatics (BMEI)*, vol. 7, pp. 569-573, 2010.
- [29] G. Zhang, and D. Feng, "Skeleton extraction of cerebral vascular image based on level set model." pp. 564-568.
- [30] T. J. Beck, F. W. Kreth, W. Beyer, J. H. Mehrkens, A. Obermeier, H. Stepp, W. Stummer, and R. Baumgartner, "Interstitial photodynamic therapy of nonresectable malignant glioma recurrences using 5-aminolevulinic acid induced protoporphyrin IX," *Lasers Surg Med*, vol. 39, no. 5, pp. 386-93, Jun, 2007.
- [31] M.Wan, Z.Liang, Q.Ke, L.Hong, I.Bitter, and A.Kaufman, "Automatic Centerline Extraction for Virtual Colonoscopy," *IEEE Transactions on medical imaging*, vol. 21, no. 12, pp. 1450-1460, 2008.
- [32] C.J.Hilditch, "Linear skeletons from square cupboards," *Machine Intelligence*, vol. 4, pp. 404-420, 1969.
- [33] M.Vermandel, N.Betrouni, C.Taschner, C.Vasseur, and J.Rousseau, "From MIP image to MRA segmentation using fuzzy set theory," *Computerized Medical Imaging and Graphics*, vol. 31, no. 3, pp. 128-140, 2007.
- [34] A. S. Dewalle-Vignion, N. Betrouni, R. Lopes, D. Huglo, S. Stute, and M. Vermandel, "A new method for volume segmentation of PET images, based on possibility theory," *IEEE Trans Med Imaging*, vol. 30, no. 2, pp. 409-23, Feb, 2011.

- [35] A. S. Dewalle-Vignion, N. Betrouni, N. Makni, D. Huglo, J. Rousseau, and M. Vermandel, "A new method based on both fuzzy set and possibility theories for tumor volume segmentation on PET images," *Conf Proc IEEE Eng Med Biol Soc*, Vancouver, Canada, 2008, pp. 3122-5.
- [36] M. Vermandel, A. S. Dewalle, P. Puech, C. Taschner, J. Rousseau, and N. Betrouni, "MRA segmentation algorithm using MIP and fuzzy set principles. Application to TOF contrast enhancement sequences," *International journal of computer assisted radiology and surgery*, pp. 104-106, 2007.
- [37] M. Vermandel, N. Betrouni, R. Viard, A. S. Dewalle, S. Blond, and J. Rousseau, "Combining MIP images and fuzzy set principles for vessels segmentation : application to TOF MRA and CE-MRA," *International Conference of the IEEE Engineering in Medicine and Biology Society*, pp. 6255-6258, 2007.
- [38] M. Naf, G. Szekely, R. Kikinis, M. Shenton, and G. Kubler, "3D Voronoï skeletons and their usage for the characterization and recognition of 3D organ shape," *Computer Vision, Graphics, and Image Processing*, vol. 66, pp. 147-161, 1997.
- [39] T. Hassan, M. Ezura, Ev. Timofeev, T. Tominaga, T. Saito, A. Takahashi, K. Takayama, and T. Yoshimoto, "Computational simulation of therapeutic parent artery occlusion to treat giant vertebrobasilar aneurysm," *American Journal of Neuroradiology*, vol. 25, no. 1, pp. 63-68, 2004.
- [40] E. W. Dijkstra, "A note on two problems in connexion with graphs," *Numerische mathematik*, vol. 1, no. 1, pp. 269-271, 1959.
- [41] I. Volkau, T. T. Ng, Y. Marchenko, and W. L. Nowinski, "On Geometric modeling of the human intracranial venous system," *IEEE Transactions on medical imaging*, vol. 27, no. 6, pp. 745-751, 2008.
- [42] I. Volkau, W. Zheng, R. Baimouratov, A. Aziz, and W. L. Nowinski, "Geometric modeling of the human normal cerebral arterial system," *IEEE Trans Med Imaging*, vol. 24, no. 4, pp. 529-39, Apr, 2005.
- [43] B. Golosio, G. L. Masala, A. Piccioli, P. Oliva, M. Carpinelli, R. Cataldo, P. Cerello, F. De Carlo, F. Falaschi, M. E. Fantacci, G. Gargano, P. Kasae, and M. Torsello, "A novel multithreshold method for nodule detection in lung CT," *Med Phys*, vol. 36, no. 8, pp. 3607-18, Aug, 2009.
- [44] Sw. Choi, and Hp. Seidel, "Hyperbolic Hausdorff distance for medial axis transform," *Graphics Models*, vol. 63, no. 5, pp. 369-384, 2001.
- [45] D. G. Altman, and J. M. Bland, "Measurement in medicine: the analysis of method comparison studies," *Statistician*, vol. 32, pp. 307-317, 1983.
- [46] J. M. Bland, and D. G. Altman, "Statistical methods for assessing agreement between two methods of clinical measurement," *Lancet*, vol. 1, no. 8476, pp. 307-310, 1986.
- [47] W. Stummer, T. Beck, W. Beyer, J. H. Mehrkens, A. Obermeier, N. Etminan, H. Stepp, J. C. Tonn, R. Baumgartner, J. Herms, and F. W. Kreth, "Long-sustaining response in a patient with non-resectable, distant recurrence of glioblastoma multiforme treated by interstitial photodynamic therapy using 5-ALA: case report," *J Neurooncol*, vol. 87, no. 1, pp. 103-9, Mar, 2008.
- [48] M. Guenot, J. Isnard, H. Catenoix, F. Mauguiere, and M. Sindou, "SEEG-guided RF-thermocoagulation of epileptic foci: A therapeutic alternative for drug-resistant non-operable partial epilepsies," *Adv Tech Stand Neurosurg*, vol. 36, pp. 61-78, 2011.
- [49] M. Cossu, M. Schiariti, S. Francione, D. Fuschillo, F. Gozzo, L. Nobili, F. Cardinale, L. Castana, and G. L. Russo, "Stereo-electroencephalography in the presurgical evaluation of focal epilepsy in infancy and early childhood," *J Neurosurg Pediatr*, vol. 9, no. 3, pp. 290-300, Mar, 2012.

- [50] M. Vermandel, A. S. Dewalle, P. Puech, C. Taschner, J. Rousseau, and N. Betrouni, "MRA segmentation algorithm using MIP and fuzzy set principles. Application to TOF contrast enhancement sequences," *Computer Assisted Radiology and Surgery, International journal of computer assisted radiology and surgery*, Berlin, Germany, 2007, pp. S104-S106.
- [51] N. Betrouni, P. Puech, A. S. Dewalle, R. Lopes, P. Dubois, and M. Vermandel, "3D automatic segmentation and reconstruction of prostate on MR images," *Conf Proc IEEE Eng Med Biol Soc*, vol. 2007, pp. 5259-62, 2007.
- [52] F. Conversano, R. Franchini, C. Demitri, L. Massoptier, F. Montagna, A. Maffezzoli, A. Malvasi, and S. Casciaro, "Hepatic vessel segmentation for 3D planning of liver surgery experimental evaluation of a new fully automatic algorithm," *Acad Radiol*, vol. 18, no. 4, pp. 461-70, Apr, 2011.